Defect-induced inhomogeneous atomic environments in complex concentrated alloys

Yuanhang Xia[a], Shuang Lyu[a], Wei Li[a,b], Yue Chen[a], Alfonso H.W. Ngan[a*]

[a] Department of Mechanical Engineering, The University of Hong Kong, Pokfulam Road, Hong Kong SAR, China

[b] Department of Engineering Mechanics, Chongqing University, Chongqing 400044, China

*Corresponding author, email: hwngan@hku.hk

Abstract:

The multiple elements in equal ratios in complex concentrated alloys (CCAs) favor the formation of local atomic environments like segregation or chemical ordering observed in recent experiments. Such special local atomic environments may pin dislocations on the slip plane, resulting in a higher flow stress for the escape of dislocations and hence a dynamic strain aging (DSA) effect in the form of stress drop. Here, Monte Carlo molecular dynamics (MC/MD) simulations are used to elucidate the atomic atmospheres around dislocations and stacking faults in the NiCoCr alloy system and quantitatively determine the stress drop effect. Increased chemical ordering and segregation around stacking faults and dislocation cores are observed, but detailed analysis shows that atomic segregation around stacking faults (Suzuki atmospheres) contributes the most to stress drop, compared with segregation around dislocation cores (Cottrell atmospheres) and enhanced ordering (Fisher) effects. The MD simulated stress drops are in good agreement with theoretically predicted and experimental values. This work fills an important gap in the understanding of the DSA effect in H/MEAs.

Keywords:

High entropy alloys; Heterogeneous atomic environments; Extended dislocations; Local pinning effects; Dynamic strain aging.

1. Introduction

Complex concentrated or high/medium-entropy alloys (H/MEAs) are solid solutions with multiple elemental species of equi-atomic concentrations (Cantor et el., 2004). Produced by quenching from a high temperature, these complex concentrated alloys were once believed to have an atomic arrangement with a high configurational entropy retained (Kaushik et al., 2021), while it is also speculated that enthalpic interactions among the various constituent elements must happen to some extent resulting in the formation of local chemical order (LCO) which is regarded as one of the major strengthening contributors for solid solutions (Antillon et al., 2020). LCO in the size range from a few angstroms to a few nanometers has indeed been observed experimentally in a number of CCAs, including CrCoNi (Zhang et al., 2020; Zhou et al., 2022), VCoNi (Chen et al., 2021), $Al_{9.5}CrCoNi$ (Wang et al., 2022) and NiCoFeCrMn (Su et al., 2022). For CrCoNi MEAs with a face-centered cubic (FCC) lattice, short-range ordered microstructures were reported following different thermomechanical processing methods, such as prolonged aging at 1273 K for 120 h (Zhang et al., 2020) or cold-rolling followed by annealing at 1273 K for 1 hour (Zhou et al., 2022). Ordered microstructures in CCAs or traditional alloys also tend to form during thermomechanical processing (Geng et al., 2023), which increases the amount of dislocations or vacancies thus providing plenty of pathways for solute diffusion to accelerate ordering and/or segregation (Snoek, 1942; Geng et al., 2023).

For conventional binary alloys, interactions between gliding dislocations and dynamically evolving solute-atomic environments are known to occur, resulting in the classical dynamic strain ageing (DSA) phenomenon manifested in terms of intermittent yield drops or serrated plastic flow (Fig. 1). These interactions include: (a) the Cottrell-Jaswon effect (Cottrell and Jaswon, 1949) (solute segregation around dislocation cores), (b) the Suzuki effect (Suzuki, 1952; Chowdhury et al., 2015) (solute segregation on stacking faults in extended dislocations), (c) the Fisher effect (Fisher, 1954; Smith et al., 2020) (extra energy required to break a short-range ordered microstructure), and (d) the Snoek effect (Snoek, 1942; Marchenko et al., 2016) (dislocation stress-field induced short-range ordering (SRO)). In CCAs, recent investigations have also revealed serrated stress-strain behavior characteristic of the DSA effect (Antonaglia et al., 2014; Tsai et al., 2019; He et al., 2021). While only one or two of the above solute-dislocation interaction effects are important in binary alloys (Bryukhanov, 2020), CCAs have much higher potential for SRO formation and hence more combinations of the interaction effects should be considered, but so far, no known study has focused on understanding the dynamic formation of atomic atmospheres around defects in CCAs and the relation to the DSA phenomenon. In particular, how the solute atoms diffuse and rearrange themselves near dislocations, and what effects this kind of *in situ* atomic rearrangements have on dislocations, are important questions to answer.

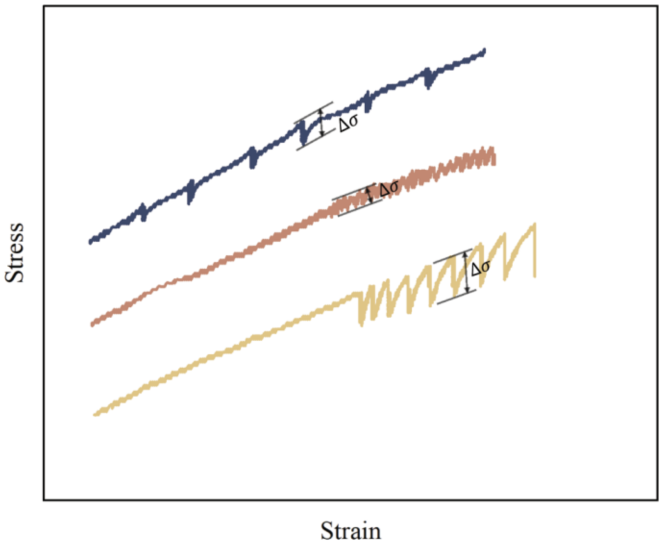

Fig. 1. Schematic illustration of stress drop Δ*σ* in stress-strain curves flow serrations.

For the above reason, in this work molecular dynamics (MD) simulations are used to elucidate the interactions between dislocations and local atomic environments in a representative MEA of NiCoCr, which is a face-centered cubic (f.c.c.) single-phase solid solution known to have a strong potential to form SRO with near-zero or even negative stacking-fault energies (SFEs) (Cantor et el., 2004; Gludovatz et al., 2016). Hybrid Monte-Carlo/molecular-dynamics (MC/MD) simulations were carried out to study the degree and distribution of SRO which were utilized to characterize the atomic environment changes in alloy replicas containing different dislocation densities at different temperatures. The simulations were performed with the Large-scale Molecular

Dynamics Massively Parallel Simulator (LAMMPS) (Plimpton, 1995) with Li et al. (2019) 's embedded atom method (EAM) potentials for the NiCoCr system in equi-atomic ratios. Previous studies have employed this set of potentials with satisfactory outcomes (Hua et al., 2021; Li et al., 2023).

The subsequent layout of the paper is as follows. In Section 2 below, we first report the MD simulated local atomic environments near dislocations and stacking faults in NiCoCr, so as to give an overall understanding of the defect-induced segregation in this alloy system. Then, in Section 3, we will simulate the strengthening due to the local atomic environments. Finally, in Section 4, we will interpret the simulated strengthening by the contributions of the abovementioned dislocation-solute interaction mechanisms (Cottrell-Jaswon, Suzuki, Fisher and Snoek), as well as to compare with experimentally observed DSA effects. The goal of this work is therefore to make use of MD simulations to rationalize the DSA effect in the prototype MEA of NiCoCr, within the classical theoretical framework of solute-defect interactions in solid-solution alloys.

2. Local atomic atmospheres near dislocations and stacking faults

2.1 Simulation setup

The simulations were performed on simulation cells defined by an orthogonal coordinate system of X = $[1\bar{1}0]$, Y = $[11\bar{2}]$, Z = $[111]$, with lengths L_x = 1300 Å, L_y = 130 Å and L_z = 123 Å, and periodic boundary conditions applied along the three directions. The simulation cells contained Ni, Co and Cr atoms of equal ratios randomly distributed in the f.c.c. structure. To simulate the effects of diverse dislocation densities at different temperatures, 0 (perfect), 1, 3 and 5 edge-dislocation dipoles of $\pm\frac{1}{2}[1\bar{1}0]$ Burgers vectors were introduced into the simulation cells as illustrated in Fig. 2(a) by using the LAMMPS function Atomsk. The dislocations were identified by the algorithm DXA, and function OVITO was used to visualize atomic configurations and analyze atomic stresses.

The samples with dislocation dipoles were initially energy minimized, followed by equilibration at the target temperature (0 K, 300 K or 600 K) for 200 ps in an NPT ensemble. Then ten MC swap attempts were made to exchange atoms in each MD step with a timestep of 1fs until the energy converged. Such a scheme ensured rapid chemistry optimization at the beginning of the simulation by the large number of (ten) MC steps per cycle, while towards the end when a sufficiently optimized chemical structure has been obtained, the MC attempts will be rejected and further structural relaxation via fine-tuning the atomic positions will be carried out by the MD step in each cycle.

To characterize the chemical ordering degree of different configurations, the Warren-Cowley parameter α is used:

$$\alpha_{\mathrm{r}}^{mn} = \frac{P_r^{mn} - c_n}{\delta_{mn} - c_n} \tag{1}$$

where P_{r}^{mn} is the probability of finding an *n*-type atom around an *m*-type atom in the 1st-nearest neighbor shell (containing 12 atoms for perfect and faulted f.c.c.), δ_{mn} is the Kronecker delta function, and c_n is the atom fraction of *n*-type atoms in the alloy. α_{r}^{mn} indicates species segregation for the following three situations:

- if α_{r}^{mn} is near zero, then *mn*-type atomic pairs are randomly distributed;
- if α_{r}^{mn} is positive when $n = m$ (the same element pair), then the same kind of atoms forms segregation;
- if α_{r}^{mn} is negative when $n \neq m$ (different species pair), then chemical ordering of these two types of atoms occurs.

It should be noted that other possible cases for α_{r}^{mn} should be consequences of the above cases. Say, if the second case above happens, then other species $n \neq m$ should be depleted around atom m, and then the corresponding α_{r}^{mn} will be positive for those species *n*. Similarly if the third case happens for one inhomogeneous species around atom *m*, then other species may be depleted with the corresponding α_{r}^{mn} being positive if $n \neq m$ or negative if $n = m$. Therefore, it is sufficient to only look for the above three cases in a given alloy situation, while other cases can be treated as consequences.

2.2 Local segregation due to dislocations

Hybrid MC/MD calculations were first conducted at 300K in cells of the same size, but containing 0, 1, 3 and 5 edge dislocation dipoles respectively, representing different dislocation densities. The potential energy per atom continuously declines with more MC swapping attempts, as depicted in Fig. 2(b). Furthermore, a detailed comparison shows an ascending trend for the initial energy (E_i) and relaxed energy (ΔE), meaning higher instability and a greater potential to develop ordered microstructures, as more dislocations are introduced into the initial configuration. Although the differences of E_i and ΔE among configurations may seem minor, they are actually significant because the number of atoms in the simulation cells is large (around 2 million). Hence, the variation in the average potential energy per atom is an important indicator for the influence of dislocations on atomic environment.

Fig. 2(c) depicts the globally averaged Warren-Cowley parameters (GAWCPs) (Xie et al., 2021) computed for all the atoms in each of the annealed configurations containing different numbers of dipoles. With different number of dislocations in the simulation cell, little variation was observed in the GAWCPs for the six atomic pairs shown. Here, the negative GAWCP for Co-Cr denotes local ordering and the positive GAWCP for Ni-Ni indicates nickel segregation, while, as explained above for eqn. (1), the WC parameters for other pairs are just consequences of the Co-Cr and Ni-Ni segregation. Say, the negative WC parameter for Cr-Cr and positive parameter for Ni-Cr indicate that Cr does not prefer to bond with Cr or Ni, and so these values are just consequences of the preferential Cr-Co paring. Similarly, the nearly-zero WC parameter for Co-Co and positive parameter for Co-Ni indicate that Co has a neutral tendency to bond with itself and strong tendency to not bond with Ni, and hence it must prefer to bond with Cr which is just what the negative WC value for Co-Cr tells. All in all, the results here indicate that only Co-Cr and Ni-Ni segregations are significant in the present simulated alloy. Furthermore, the results in Fig. 2(c) also show that dislocation density barely affects the average degree of global ordering.

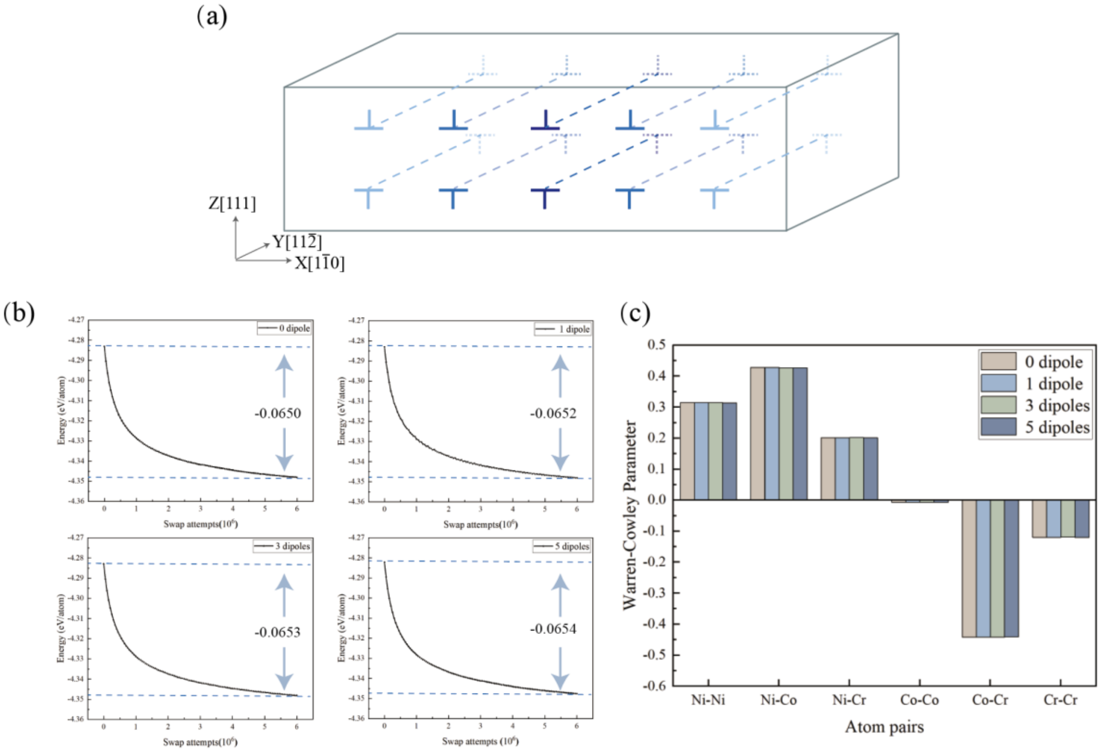

Fig. 2. MC/MD simulations of NiCoCr alloy with different dislocation densities. (a) Sketch of the simulation box and the inserted dislocation dipoles. (b) Potential energy vs swap attempts for systems containing: 0(perfect), 1, 3 and 5 edge dislocation dipoles. (c) Globally averaged Warren-Cowley parameters of Ni-Ni, Ni-Co, Ni-Cr, Co-Co, Co-Cr and Cr-Cr atom pairs in the MC-relaxed samples with different numbers of dipoles.

However, previous reports in the literature have assumed that the presence of a stress field would influence atomic diffusion and local atom rearrangement (Song et al., 2018), and so the ordering degree would be expected to differ between the slip plane and the compressive and tensile regions of dislocation stress fields. Fig. 3 shows an investigation on the locally averaged Warren-Cowley parameters (LAWCPs). Here, the simulation cell is divided into 10 layers each 12 Å thick along the Z [111] axis as shown in Fig. 3(a), and the Warren-Cowley parameter of each layer is then computed to determine the Co-Cr SRO distribution.

Fig. 3(b) compares the ordering distributions along Z in systems with various dislocation densities. For all three defected structures, the WC-SRO parameter experiences a sudden change near the 3rd and 8th layers where dislocations reside. Co-Cr exhibits the highest ordering (more negative WC parameter) near the two slip planes, with higher ordering levels in the compressive regions (1st, 2nd, 9th and 10th layers) than the tensile regions (4th, 5th, 6th and 7th layers) of the dislocation stress fields. The inhomogeneity of ordering degree becomes increasingly obvious with increasing dislocation density, and the fluctuation amplitude of the WC parameter reaches a maximum value of approximately 0.038 in the 5-dipole configuration. Besides, Fig. S1 shows the detailed value of the WC parameters for six atomic pairs in layers of the 300K-annealed, 5-dipole sample, where it can be seen that the stress distribution has little influence on the formation of the types of atomic pairs.

To eliminate the effect of layers chosen for insertion and confirm the existence of the non-uniform ordering phenomenon, in another simulation the 3rd, 4th and 5th layers were selected respectively to insert negative dislocations while keeping the 8th layer for insertion of positive ones. The results in Fig. S2(a) display the same variation trend for the WC-SRO parameter. Furthermore, it is found that as the two slip planes approach one another, the minimum value of the WC parameter α_{min} becomes higher meaning less ordering which is related to the variation of the stress field. The hydrostatic stress was calculated for every atom and averaged for each layer as shown in Fig. S2(c). As the slip planes are brought closer, the peak stress, valley stress and stress on the slip planes become more positive due to the superposition of the stress fields of the dipoles. The result here further confirms that, as a rule in the present simulated alloy, SRO is more likely to form in compressive regions. Besides, Fig. S2(d) demonstrates that the hydrostatic stress gradient gradually increases with more dipoles inserted, which also agrees well with the rule. Moreover, the simulation cell was redivided into 30 layers to check the influence of the chosen layer thickness (atoms counted in different layers), and yet, as evidenced by Fig. S2(b), the ordering phenomenon remains unchanged.

The ordering inhomogeneity can be indicated by the WC-SRO variation amplitude $\Delta\alpha$ ($\Delta\alpha = \alpha_{max} - \alpha_{min}$) along the Z direction. The WC-SRO parameter evolution during MC/MD relaxation is depicted in Fig. 3(c). As the Monte Carlo exchange steps increase, the atomic ordering increases. Besides, the temperature and dislocation density dependence on $\Delta\alpha$ were investigated as shown in Fig. 3(d), which indicates that at higher temperatures or in systems with high densities of dislocations, the level of short-range ordering near and far away from dislocations witnesses a greater difference. The reason for this is due to the higher gradients of the superimposed stress fields of the dislocations at a higher temperature, which changes the equilibrium positions of the Shockley partials in the dipoles via reduction in the stacking fault energy, as indicated by the variation of the separation between Shockley partials shown in Fig. S2(f).

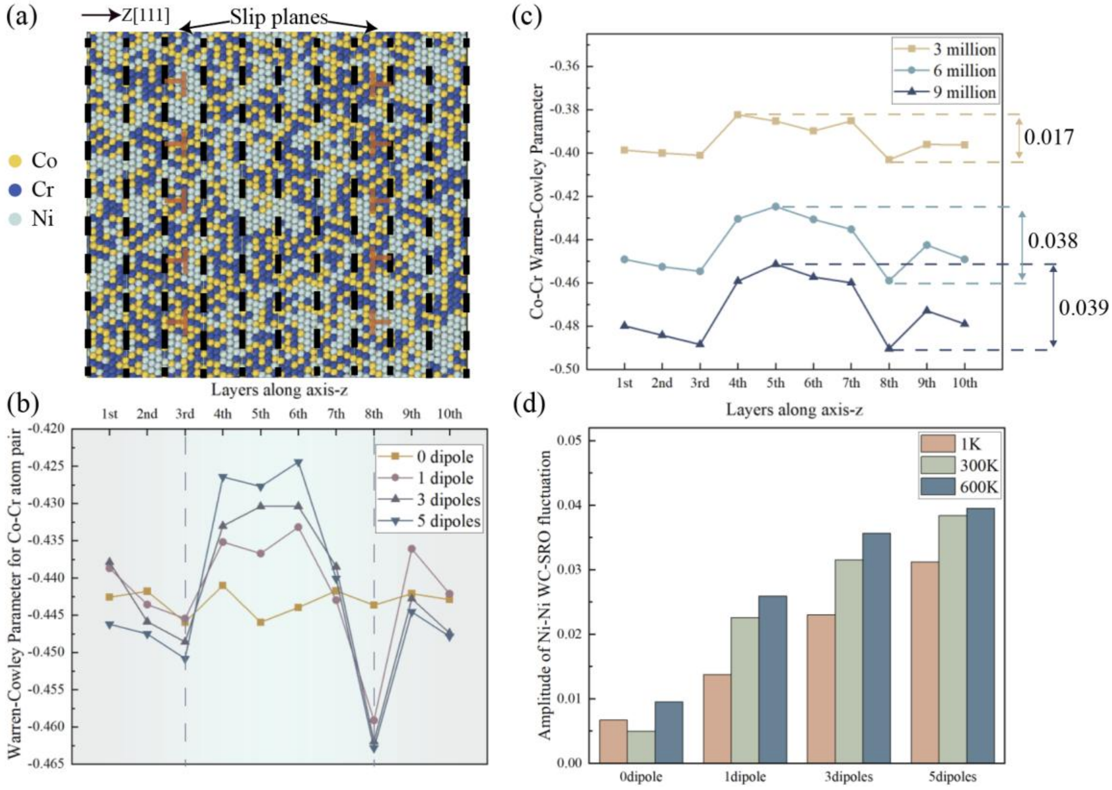

Fig. 3. Inhomogeneous distribution of ordering level for layers parallel to the slip plane. (a) Sketch of how to divide the cells for studying atom environment distribution. Each layer with an equal thickness of about 6 atom planes and dislocation dipoles lie on the 3rd and 8th layers. (b) Local Warren-Cowley parameters of Co-Cr atom pair calculated for regions in 300K-annealed samples with: 0 dipole (perfect), 1 dipole, 3 dipoles and 5 dipoles of dislocations. (c) Evolution of the heterogeneity with increasing swapping attempts. (d) Effect of annealing temperature on fluctuation amplitude of Co-Cr WC-SRO level.

2.3 Local segregation in stacking-fault regions

Fig. 4(a) reveals the segregation of Ni in the compressive regions of dislocation stress fields as well as on the slip plane (reaching the highest Ni concentration), and depletion in the tensile regions of dislocation stress fields. An analysis of the segregation on the slip plane was conducted and Fig. 4(b) illustrates a rising trend of the Ni ratio towards a saturation value of approximately 38% in the stacking-fault area on increasing MC attempt steps, with Ni (orange atoms) in the stacking fault region (Co or Cr indicated by blue atoms) shown in the insets. To further show the distinction between the defected and perfect areas, about 50 cubic pixels along $[1\bar{1}0]$ with a cross-sectional size of 25 Å × 3 Å were picked in one slip plane of the annealed 5-dipole configuration, and the Ni concentration is plotted vs X coordinates in Fig. 4(c). It can be seen that Ni adopts the equi-atomic percentage in the f.c.c region but a significantly high percentage in the h.c.p (stacking-fault) regions. These findings indicate that the Suzuki effect is clearly present in the equilibrated configurations of the present alloy system.

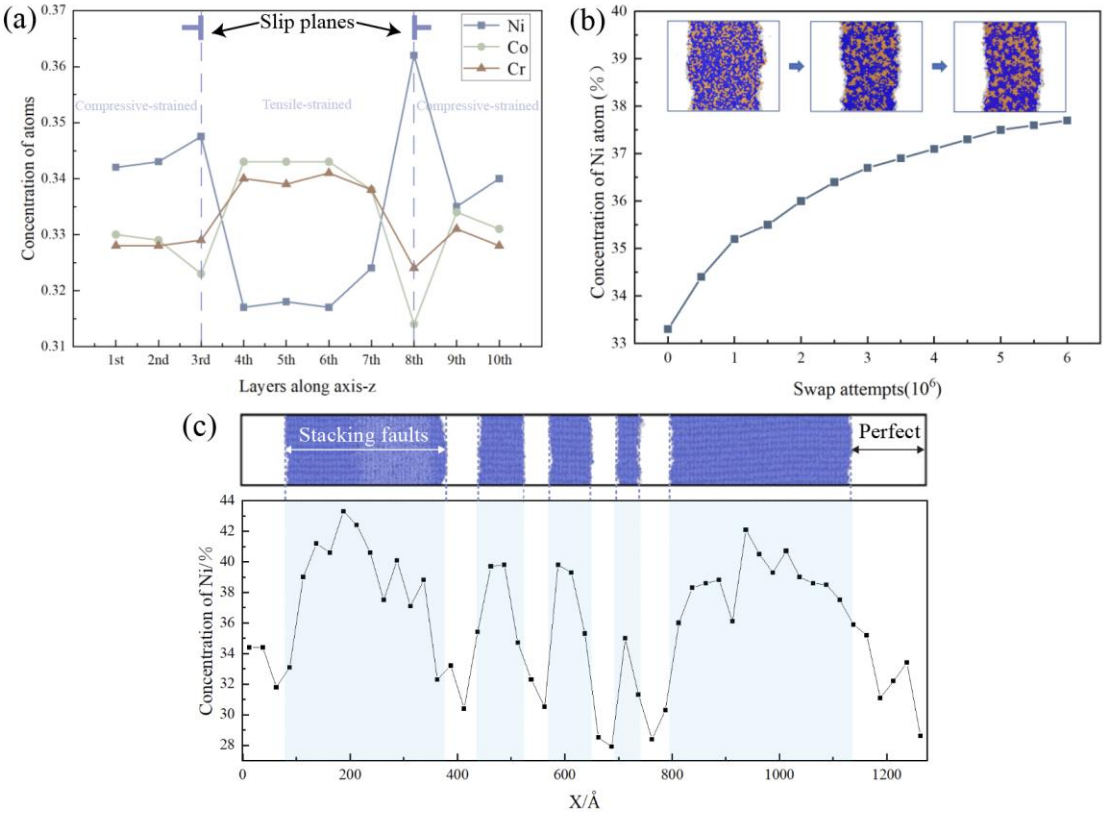

Fig. 4. Segregation of Ni in stacking faults area. (a) Concentration distribution of Ni, Co and Cr in different layers along Z [111] coordinate. (b) Ratio of Ni (orange atoms) in stacking-fault area (blue atoms) vs swap attempts in the 5-dipole configuration. (c) Planar distribution of Ni

concentration on (111) slip plane in the 300K-annealed sample along the X $[1\bar{1}0]$ direction. Only atoms in stacking-fault areas are presented and colored blue.

2.4 Dislocation line shape and local atom environment change

Next, how the local atomic environments on the slip plane affect dislocation lines is examined. Here the average curvature K_{ave} and the maximum curvature K_{max} of a given dislocation line are used to quantitatively describe the shape evolution of dislocations during MC/MD swapping process. K_{ave} and K_{max} were calculated for each of 20 dislocation lines to obtain ensemble averages $\overline{K_{ave}}$ and $\overline{K_{max}}$ before relaxation and after annealing at 300K in the system containing 5 dipoles. The results are displayed in Fig. 5, where the initially perfect straight dislocation lines dissociate into two partials and become extremely curvy at the early stage, and then both K_{ave} and K_{max} decrease and tend to stabilize with increasing MC/MD steps, indicating that the dislocations become straighter to relax their line energy while interacting with the newly formed atomic environments on the slip plane.

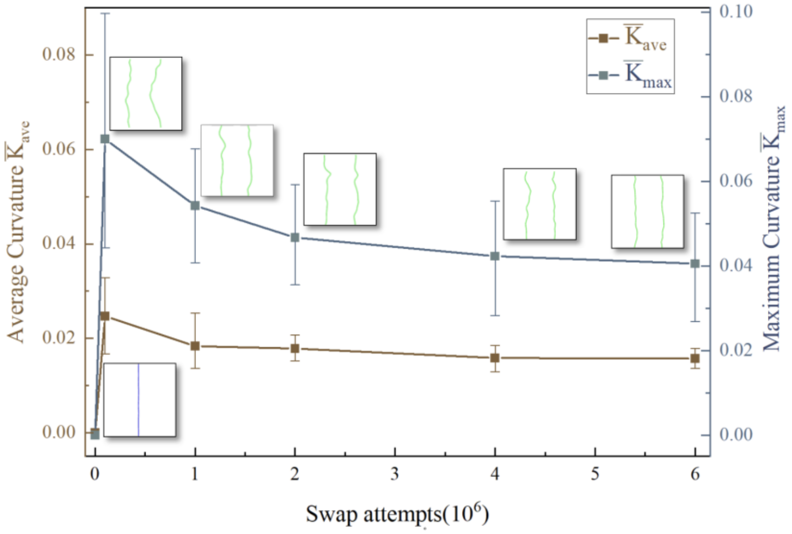

Fig. 5. Evolution of dislocation line shape and curvature in the 5-dipoles samples during the 300K-annealing process. The purple dislocation refers to a perfect $1/2[1\bar{1}0]$ edge dislocation, then dissociated into two green Shockley partial dislocations.

The above evolution in line geometry implies the formation of some unique potential atom environments close to the dislocation cores, such as Cottrell and Snoek atmospheres. To examine such local atomic environments, cylindrical volumes with radius R surrounding the dislocation cores were designated, as demonstrated in Fig. 6(b). Atom concentrations are extracted from regions with R ranging from 1 b to 3 b ($b = 1/2[1\bar{1}0]$) and the results in Fig. 6(a) show that when $R = 1b$, the Ni concentration is lower than that of Co and Cr. This disparity gradually decreases as R rises until 3 b, at which point the difference becomes negligible. This local depletion of Ni within dislocation cores corresponds to the existence of the Cottrell-Jaswon effect.

To ascertain whether the Snoek effect exists, the Co-Cr W-C parameter α near the dislocation core was computed. The averaged WC-SRO parameters for 10 dislocation lines in the initial unannealed configuration are plotted against R from 1 b to 10 b in order to eliminate the size effect on the WC-SRO data, as shown in Fig. 6(c). When $R = 1$ b, some of the $|\alpha|$ values are far away from 0, and on increasing R, most $|\alpha|$ values tend to decline and then stabilize close to 0 for $R \geq 4$ b. Compared to the WC-SRO parameter (-0.1 ~ -0.5) in annealed configurations, the error caused by the region size is negligibly low when $R \geq 4$ b. The WC-SRO parameters in the 300 K-annealed configuration were then further calculated for 10 dislocations to see the variation trend of the spatial ordering level; however, it turns out that no consistent fluctuation trend is observed when $R = 1$ to 3 b, and the variation is also negligible for $R \geq 4$ b as shown in Fig. 6(d), suggesting that there is no Snoek ordering.

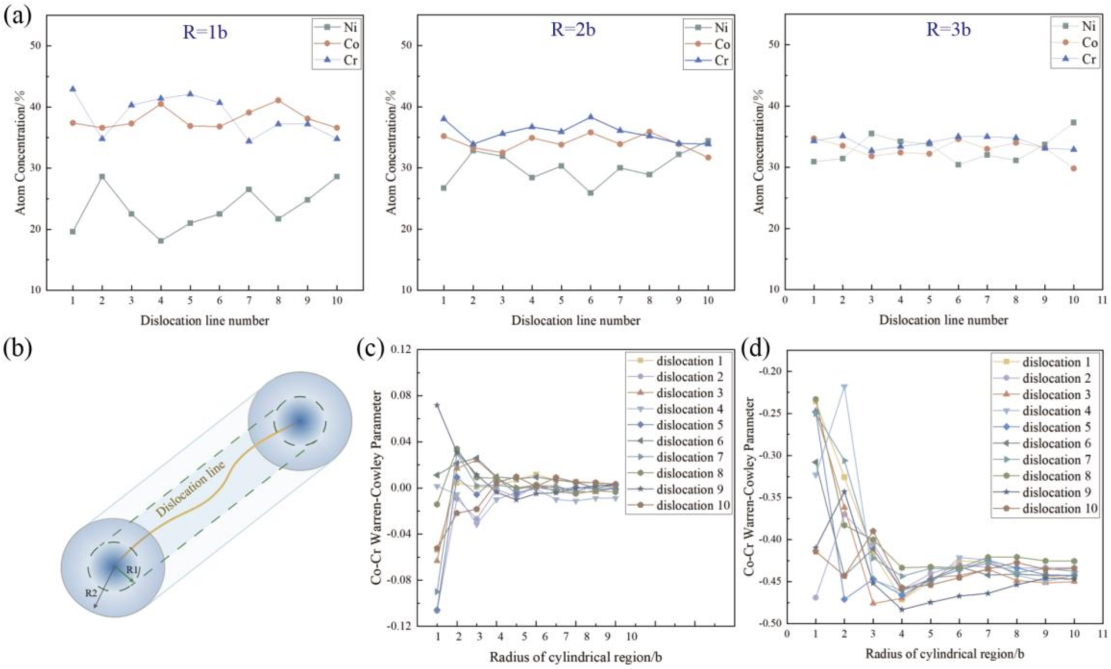

Fig. 6. Local atomic environment investigation near the dislocation core. (a) Ni, Co and Cr atom ratios in cylindrical regions with radius R ranging from 1 b to 3 b in random configuration. (b) Sketch of dislocation line and surrounding cylindrical region with different R picked for calculation of atom concentration and Warren-Cowley parameter. Warren-Cowley parameter of Co-Cr atom pair vs radius of cylindrical regions in (c) initial unannealed configuration and (d) 300 K-annealed configuration.

2.5 Interpretation of local atomic atmosphere formation

Misfit energy change of atoms due to the stress fields of dislocations or crystal-structure modifications of stacking faults (h.c.p. vs f.c.c.) is expected to be responsible for the heterogeneous atomic distribution around these defects. As given by eqn. (2) below, the elastic interaction energy between a solute and an edge dislocation is the product of the hydrostatic component of the dislocation stress field p (in polar coordinates (r, θ)) and the solute misfit volume ΔV (Záležák et al., 2017):

$$E = p\Delta V = \frac{4(1+\nu)Gbr_p^3\delta}{3(1-\nu)}\frac{\sin\theta}{r} \tag{2}$$

where ν denotes Poisson's ratio. The misfit volume $\Delta V = 4\pi r_p^3\delta$, in which r_p and represent the radii of the atom, and δ is a misfit parameter which is a volume change factor in Eshelby's misfitting sphere model (Hull et el., 1984). For the present MEA system, the radii of Ni, Co and Cr are 115, 116 and 118 pm, respectively. According to eqn. (2), for the random configuration, the presence of Ni (the smallest atom) in a region below the slip plane of an edge dislocation would take a positive δ, as would the presence of Co or Cr (larger atoms) in a region above the slip plane. So in the initial unannealed MEA with a high misfit strain energy, a large driving force is then yielded to cause solute atoms to segregate to appropriate locations and lower the energy. As a result, in an annealed state, the concentration of Ni in the compressive regions of dislocation fields is larger than that in tensile regions as shown in Fig. 4(a), while the case for Co and Cr is reversed.

Moreover, as illustrated in Fig. 3(b), the introduction of greater amounts of dislocations into the original configuration tends to enhance the maximum Co-Cr ordering level and its spatial variation amplitude. The superposition of the dislocation stress fields is the most likely cause of the enhanced ordering. Hence, the hydrostatic stress was calculated and recorded for each atom during the simulation process in the 5-dipole configuration. The considerable distinction between the tensile and compressive regions in the unannealed random state is shown by the hydrostatic stress distribution over a cross section perpendicular to the dislocation line in Fig. 7(a). The amplitude of the hydrostatic stress variation tends to decrease with increasing MC/MD steps, as illustrated in Fig. 7(b) and (c), accompanied by the formation of inhomogeneous Co-Cr ordering. Therefore, it is plausible to conclude that the formation of this type of new atomic environments contributes to the relaxation of internal stress and energy of the alloy.

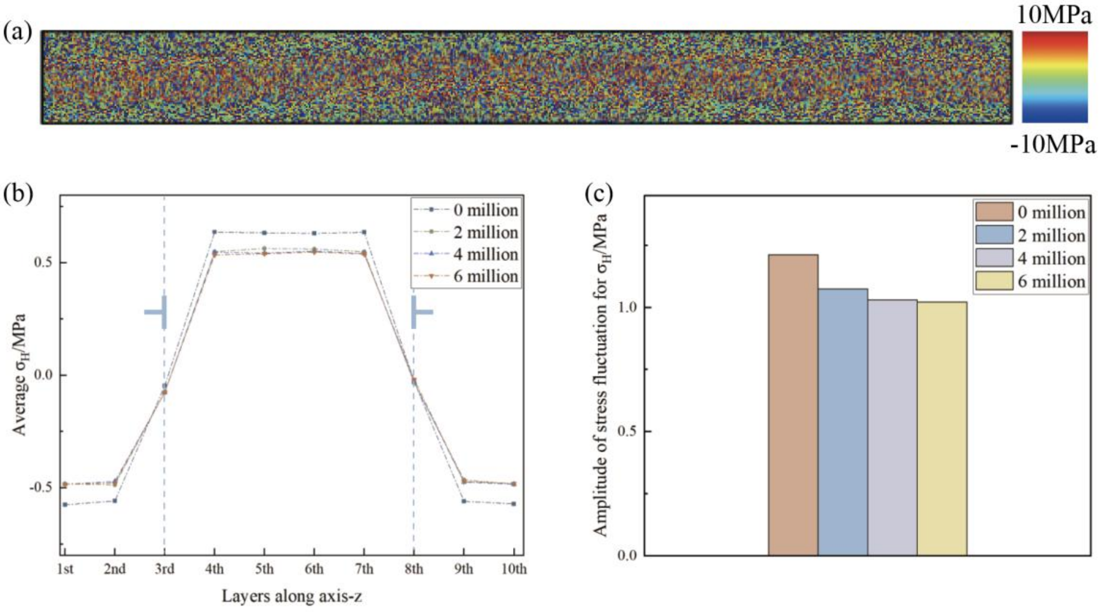

Fig. 7. Stress distribution evolution in the sample inserted with 5 dipoles. (a) Atomic hydrostatic stress distribution. (b) Hydrostatic stress profiles at increasing MC/MD steps. (c) The hydrostatic stress fluctuation amplitudes at increasing MC/MD steps.

Besides, the results in Fig. 4(c) show Ni segregation in stacking faults resembling the Suzuki effect, a type of chemical interaction in which substitutional solutes migrate to stacking faults to reduce their specific energy. Additionally, Fig. 6(a) shows Co and Cr segregation to dislocation cores, resembling Cottrell atmospheres driven by the energy decrease for elastic interaction between dislocation stress fields and solute atoms. Meanwhile, the Suzuki (stacking-fault) segregation may offer the Co and Cr species more opportunities to interact to produce short-range ordered microstructures, which may explain why the Co-Cr ordering level is quite high on the slip plane as shown in Fig. 3(b). Compared to the homogeneous atomic environment, the appearance of such a higher ordering level on the slip plane, as opposed to the homogeneous atomic environment, may produce a resistance effect on dislocation motion, which we call the Fisher effect below.

3. Strengthening due to local atomic atmospheres

Having established the local atomic atmospheres near dislocations and stacking faults in NiCoCr, in this section we study their strengthening effects by carrying out further simulations on dislocation resistance with and without formation of such atmospheres. The simulation cells for this purpose had the same coordinate system as in Section 2, i.e. X = $[1\bar{1}0]$, Y = $[11\bar{2}]$, Z = [111], but were larger with lengths L_x = 1700 Å, L_y = 450 Å and L_z = 123 Å to reduce the size effect and provide a broad slip plane for the accurate calculation of critical resolved shear stress. For stress application, thin boundary slabs of thickness 12 Å are set on the top and bottom in the Z direction of the simulation cell, while the remaining middle region is treated as the main simulation region.

Model	Brief	Full Description
M	Master	Along X = $[1\bar{1}0]$, Y = $[11\bar{2}]$, Z = [111], with lengths L_x = 1700 Å, L_y = 450 Å and L_z = 120 Å. Ni, Co, and Cr atoms were randomly distributed in equal ratio into the f.c.c. structure, and followed by energy minimization at 0K and then further relaxation at 300 K for 200 ps using NVT ensemble. A top and a bottom layer each of thickness 12 Å in the Z direction were set as boundary layers, while the remaining middle region was treated as the main simulation region.
C	Constrained dislocation introduced after MC relaxation	Starting from Model M, MC/MD exchange was performed in the main simulation region: 10 MC swap attempts per MD step, and then equilibration at 1 K for 200 ps. Then, an edge dislocation with Burgers vector $\frac{1}{2}[1\bar{1}0]$ was introduced in the cell center, followed by energy minimization and relaxation at 1 K for 200 ps to allow the dislocation to dissociate.
R1	Single dislocation relaxed by MC	Starting from Model M, an edge dislocation with Burgers vector $\frac{1}{2}[1\bar{1}0]$ was introduced in the cell center, followed by MD energy minimization at 1 K for 200 ps. Then MC/MD exchange was performed in the main simulation region: 10 MC swap attempts per MD step, and then equilibration at 1 K for 200 ps.
R10	Five dipoles relaxed by MC	Starting from Model M, 5 edge dipoles of Burgers vectors $\pm\frac{1}{2}[1\bar{1}0]$ were introduced in the cell, followed by MD energy minimization at 1 K for 200 ps. Then MC/MD exchange was performed in the main simulation region: 10 MC swap attempts per MD step, and then equilibration at 1 K for 200 ps.

Table 1 – Summary of the MD models used for simulating strengthening due to local atomic atmospheres.

As strengthening due to local atomic atmospheres requires the comparison of dislocation resistance (critical resolved shear stress) with and without the atmospheres formed, two MD models, C and R1 as summarized in Table 1, were used for this purpose. The difference between C and R1 lies in the sequence of dislocation introduction and MC exchange – C, the constrained model, had the MC exchange done before dislocation introduction, while R1, the relaxed model, had the reverse. The difference between these two configurations then allowed the effects of local atomic atmospheres around the dissociated dislocation to be revealed. The two models C and R1 were then subjected to a gradually increasing shear stress (20 MPa per 100 ps) applied at their boundary layers at 1 K, where periodic boundary conditions were applied along the X and Y directions. To determine the flow stress, the positions of the Shockley partials and applied shear stress were recorded in both samples. Then the stress drop, denoted as $\Delta\tau_S$, was quantified as the difference between the flow stresses in models C and R1.

The simulated result in Fig. 8(a) shows that in Model R1, the leading partial keeps static for the first 5500ps and then starts to slip continuously when the applied stress is 945 ± 14 MPa, while the trailing partial gets rid of pinning at a higher shear stress of about 983 ± 10 MPa. Besides, as shown in Fig. S3, in Model R1 the trailing partial does not move until the leading partial passes through the box, re-enters the simulation cell from the left and approaches it from behind, and then in the next 100ps the two partials move together as a group, maintaining a small, constant spacing of about 10nm. This suggests that the mutual dislocation interaction force also contributes to the critical resolved shear stress (τ_{CRSS}) needed to move the partials. τ_{CRSS} and the interaction stress ($\tau_{interaction}$) on dislocation j due to another dislocation i are given by (Wang et al., 2022):

$$\tau_{CRSS} = \tau_{Simulation} \pm \tau_{interaction} \tag{3}$$

$$\tau_{interaction} b_j = \frac{\mu}{2\pi R_{ij}}(\boldsymbol{b_i}\cdot\boldsymbol{\xi})(\boldsymbol{b_j}\cdot\boldsymbol{\xi}) + \frac{\mu}{2\pi(1-\nu)R_{ij}}\left[(\boldsymbol{b_i}\times\boldsymbol{\xi})\cdot(\boldsymbol{b_j}\times\boldsymbol{\xi})\right] \tag{4}$$

where $\tau_{Simulation}$ is the resolved shear stress applied to the simulation cell when the dislocation starts to move, i.e. the uncorrected critical resolved shear stress without considering interactions from other dislocations in the system. Here, the interaction force arises from the radial force F_r between the dislocations because the dislocation lines lie on the same plane. Burgers vectors $\boldsymbol{b_i}$ and $\boldsymbol{b_j}$ can be either for the leading $\frac{a}{6}[\bar{1}2\bar{1}]$ or trailing $\frac{a}{6}[\bar{2}11]$ dislocations. Dislocation line direction $\boldsymbol{\xi}$ is $\frac{1}{\sqrt{6}}[11\bar{2}]$, and $\boldsymbol{R}$ is the unit vector pointing from dislocation i to j determined by their relative positions.

After correcting for the interaction stress, the final τ_{CRSS}^{R1} is 945 ± 14 MPa for the leading partial and 1104.8 ± 10 MPa for the trailing partial in Model R1. While for Model C, Fig. S4 shows discrete displacements of the two partials under low shear stress. Continuous slip occurs when the shear stress approaches 800 ± 12 MPa for the leading one and 950 ± 8 MPa for the trailing one, as depicted in Fig. 8(b) and Fig. S4. Contrary to the slide behaviors in Model R1, the two partials in Model C do not move forward together and the trailing one could continue advancing even when the spacing increases a lot. In consequence, we can neglect the effect of interaction force in Model C and the final τ_{CRSS}^{C} is just the $\tau_{Simluation}$ of 802 ± 12 MPa for the leading partial and 950 ± 8 MPa for the trailing partial. Consequently, the stress drop $\Delta\tau = \tau_{CRSS}^{R1} - \tau_{CRSS}^{C}$ is calculated to be approximately 143 MPa and 154 MPa for the leading and trailing partial, respectively.

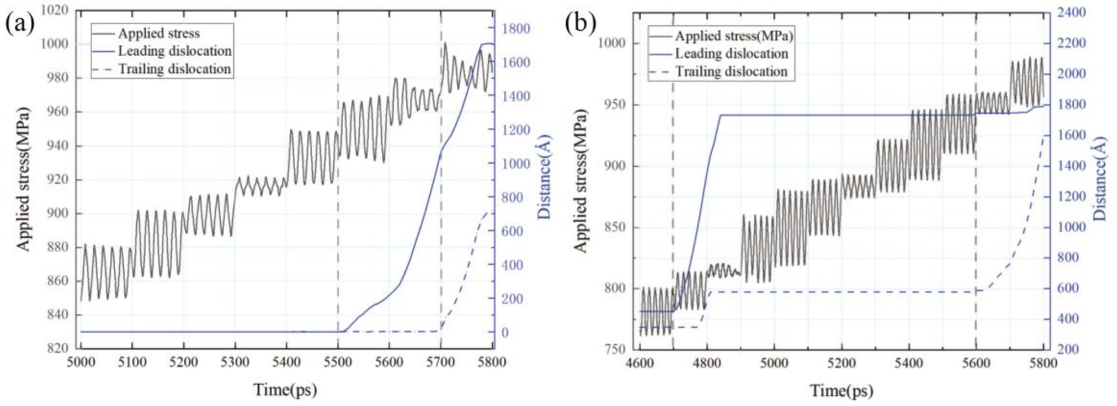

Fig. 8. Simulation of dislocation slide process under applied shear stress. Applied stress (black curve), displacement of leading partial (blue curve) and trailing partial (blue dotted curve) dislocations vs loading time in (a) Model R1 (dislocation relaxed by MC/MD) and (b) Model C (constrained dislocation not relaxed by MC/MD).

4. Interpretation of segregation induced strengthening by the Suzuki, Fischer and Cottrell-Jaswon mechanisms

Here in this section, we analyze and predict the strengthening contributions of each of the Suzuki, Fischer and Cottrell-Jaswon solute segregation mechanisms mentioned in Section 1, aiming to rationalize the MD simulated strengthening in Section 3 as well as experimental observations in the literature. Recalling that the Snoek effect is absent in the present NiCoCr system (Fig. 5(d)), this is not considered here.

4.1 Suzuki effect

The Suzuki effect refers to the segregation of substitutional atoms onto stacking faults of extended dislocations in f.c.c. crystals, causing lowering of the free energy F per unit area of the stacking fault (Suzuki, 1952). Suppose that in a system with an average solute concentration of c_1, segregation happens in the stacking fault area bounded by two partial dislocations with a solute concentration of c_2. Under applied stress $\boldsymbol{\sigma}$, force balance of the two partials at equilibrium positions x_1 and x_2 is represented as:

$$\frac{A}{x_2 - x_1} = \begin{cases} 2h(\Delta F_V)_{c_1} - (\boldsymbol{\sigma} \cdot \boldsymbol{b_L}) \cdot \boldsymbol{n} & \text{for leading partial} \\ 2h(\Delta F_V)_{c_2} + (\boldsymbol{\sigma} \cdot \boldsymbol{b_T}) \cdot \boldsymbol{n} & \text{for trailing partial} \end{cases} \quad (5)$$

$$\boldsymbol{b_T} + \boldsymbol{b_L} = \boldsymbol{b} \quad (6)$$

$$(\boldsymbol{b} \cdot \boldsymbol{\sigma}) \cdot \boldsymbol{n} = \tau b \quad (7)$$

Here, $A/(x_2 - x_1)$, where $A = \frac{\mu a^2 (2+\nu)}{48\pi(1-\nu)}$, is the repulsive force between the two partials, μ is shear modulus, ν is Poisson's ratio, and a is lattice constant. Furthermore, $\boldsymbol{b_T}$, $\boldsymbol{b_L}$ and $\boldsymbol{b}$ are respectively the Burgers vector of the leading partial, trialing partial and the total dislocation, h is the thickness of the h.c.p layer for the stacking fault, ΔF_V is the difference in free energy per unit volume between the f.c.c. and h.c.p. structure so that $2h(\Delta F_V)_{c_1}$ and $2h(\Delta F_V)_{c_2}$ represent the force due to the stacking fault for alloy states with solute concentration c_1 and c_2, respectively, and the term $(\boldsymbol{\sigma} \cdot \boldsymbol{b}) \cdot \boldsymbol{n}$ refers to the force exerted by the external stress field, with $\boldsymbol{n}$ being the unit vector normal to the slip plane. In eqn. (7), τ is the resolved shear stress in the slip system due to $\boldsymbol{\sigma}$, and b is the magnitude of $\boldsymbol{b}$. Therefore, combining eqn. (5) with (6) and (7), Suzuki segregation offers the following critical stress which needs to be overcome for moving the partial dislocations:

$$\Delta\tau_{Suzuki} = \frac{2h}{b}\left|(\Delta F_V)_{c_1} - (\Delta F_V)_{c_2}\right| = \frac{1}{b}\left|(\gamma_{SFE})_{c_1} - (\gamma_{SFE})_{c_2}\right| \tag{8}$$

where $\gamma_{SFE} = 2h\Delta F_V$ is the stacking fault energy (SFE).

To calculate $\Delta\tau_{Suzuki}$ from eqn. (8), the $(\gamma_{SFE})_{c_1}$ and $(\gamma_{SFE})_{c_2}$ are estimated by further MD simulations. $(\gamma_{SFE})_{c_1}$ is acquired from Model M in Table 1 with evenly distributed Ni, Co and Cr atoms of equal ratios, by performing rigid displacement of the upper half the simulation cell against the lower half along the <112> directions and then relaxation along Z direction and calculating the energy difference. For the estimation of $(\gamma_{SFE})_{c_2}$, Model R10 in Table 1 was employed, from which the equilibrium dislocation positions of 5 dislocation dipoles relaxed by MC were used to estimate the stacking-fault energy after local atomic atmosphere formation. The use of 5 dipoles (i.e. 10 full dislocations) here, instead of just one dislocation in Model R1, is to increase the total area of stacking-fault ribbons in the simulation cell so as to increase the accuracy of the calculated γ_{SFE}. Nevertheless, Fig. S5(a) shows that the concentrations of Ni atoms in Model R1 and R10 after 7 million MC exchange attempts are comparable. Then, assume that only the repulsive forces between dislocations and the forces from stacking faults act on the dislocation lines, while friction stress is negligible due to the strong interactions within a high density of dislocations and periodic boundary conditions along all the three directions. Also, as depicted in Fig. 5, the curvature of these dislocation lines became quite low after annealing so we can make the further assumption that these dislocation lines are nearly parallel to each other. Then, for any two dislocations *i* and *j* of Burgers vectors $\boldsymbol{b_i}$ and $\boldsymbol{b_j}$ separated by distance

R_{ij} in the array, the interaction force can be given by (Wang et al., 2022):

$$F_r^{ij} = \frac{\mu}{2\pi R_{ij}}(\boldsymbol{b_i} \cdot \xi)(\boldsymbol{b_j} \cdot \xi) + \frac{\mu}{2\pi(1-\nu)R_{ij}}[(\boldsymbol{b_i} \times \xi) \cdot (\boldsymbol{b_j} \times \xi)] \quad (9)$$

$$F_\theta^{ij} = \frac{\mu}{2\pi(1-\nu){R_{ij}}^3}\{(\boldsymbol{b_i} \cdot \boldsymbol{R})[(\boldsymbol{b_j} \times \boldsymbol{R}) \cdot \xi)] + (\boldsymbol{b_j} \cdot \boldsymbol{R})[(\boldsymbol{b_i} \times \boldsymbol{R}) \cdot \xi] \quad (10)$$

where F_r^{ij} and F_θ^{ij} are respectively the radial and circumferential components of the interaction force as depicted in Fig. 9(b). A cut-off radius of 1724 Å (equal to the length of the simulation box) was chosen, and dislocations within the region were regarded to interact with one another as shown in Fig. 9(c). The interaction forces $F_r^{ij}$and F_θ^{ij} on dislocation i from another dislocation j in the system can be decomposed into component F_x^{ij} along the X direction, counterbalancing the adjourning stacking fault with SFE γ_i:

$$F_x^{ij} = F_r^{ij} \cos\alpha + F_\theta^{ij} \sin\alpha \quad (11)$$

$$\sum_{j=1}^{n}(F_x^{ij} \pm \gamma_i) = 0 \quad \text{for dislocation } i \quad (12)$$

The stacking fault energy $\bar{\gamma}$ of the alloy state can then be estimated as the average value of the γ_i calculated for dislocation i = 1, 2 … 10 in the system. The SFE values calculated using eqn. (12) using the relaxed dislocation positions from the present MD simulation for the random perfect configuration are given in Table S1. It turns out that the average -17.3 mJ/m^2 for $\bar{\gamma}$ agrees well with the range of -14.4 to -20.0 mJ/m^2 from Li et al. (2023) ’s simulation results. The SFEs calculated from dislocation positions using eqn. (12) for Model R10 and the MD simulated fault energy curve by shearing Model M along <112> are displayed in Fig. 9(d) for comparison. The results show that $(\gamma_{SFE})c_2$ from Model R10 is 2.4 mJ/m^2, while $(\gamma_{SFE})c_1$ from shearing Model M along <112> is significantly higher at approximately 30.9 mJ/m^2. This comparison reveals that the SFE decreases significantly as a result of Ni atom segregation after relaxation by

MC exchange. Using eqn. (8), with b being a perfect 1/2<110> vector and $a = 3.558$ Å, and we get $\Delta\tau_{Suzuki} = 113.4$ MPa.

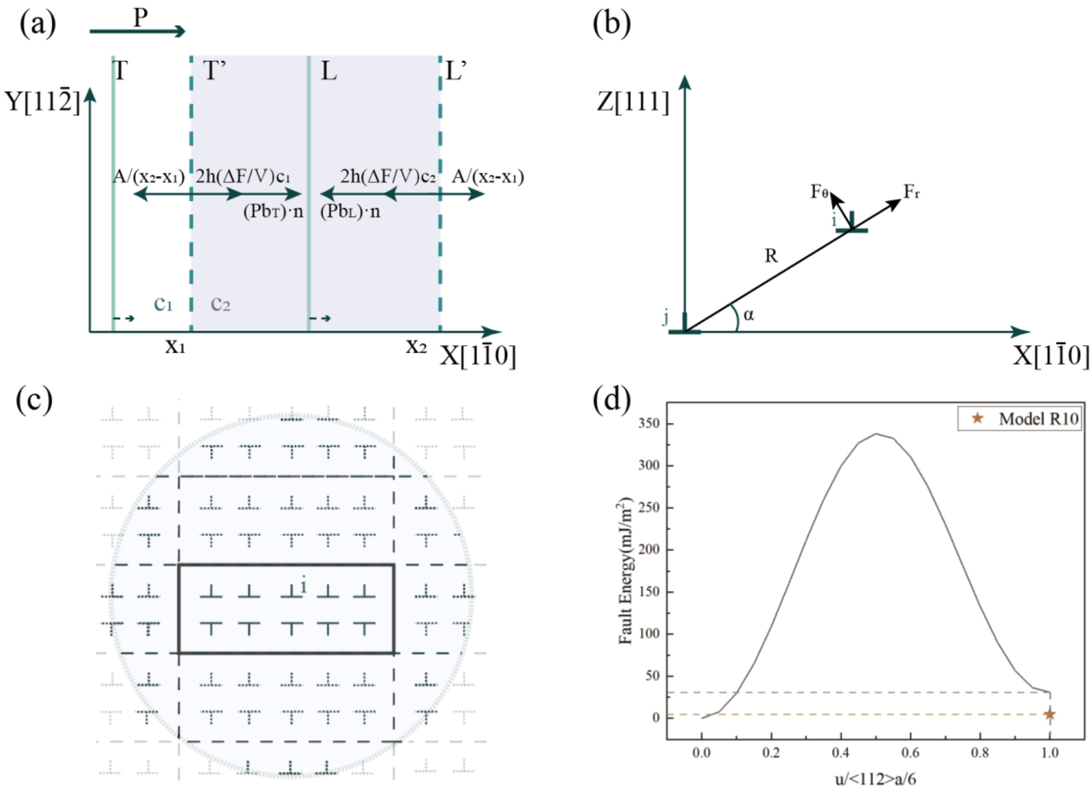

Fig. 9. Estimation of Suzuki effect on the stress drop. (a) Stress analysis for parallel leading and trailing partial dislocations. (b) Radial and circumferential interaction force between dislocation i and j. (c) Dislocations to be considered for γ_i calculation within a cutoff of R. (d) General stacking fault landscape by shearing Model M along <112> (black line), compared with γ_{SFE} calculated from Model R10 (brown dot).

4.2 Fisher effect

Hardening in ordered alloys was traditionally attributed to the hypothesis that dislocation passage could break low-energy atomic bonds and replace them by high-energy ones (Fisher, 1954), while later it was argued that the atom-dislocation interaction energy also varied during the glide of dislocations to result in a softening effect (Abu-Odeh et al., 2022). Both types of forces may compete and determine the final effect on dislocation movement. In the CrCoNi system, previous studies have validated the SRO strengthening effect (Li et al., 2023) and the destruction of atom pairs is representative of mechanical property enhancement. As suggested by Cottrell, successive glide of dislocations may produce less and less ordering along the slip plane to form more random atomic environment (Kang et al., 2014), while another possibility proposed by Cohen and Fine (Fisher, 1954) is that the degree of local ordering may not decline after several times of glide due to the atom rearrangement.

In the present material system, Co-Cr ordering is the main pinning factor, so the Co-Cr Warren-Cowley parameter α of the slip plane was recorded during the glide of dislocations to see the change. In order to examine the effect of dislocation passage on short-range ordering microstructure, α is calculated by only retaining the two layers of atoms on the slip plane to detect the breakage or reconnection of atomic pair bonding. As shown in Fig. 10, after about 2 to 3 dislocation passes through the box, the SRO level reaches the minimum value of near zero, which means a near-random state. For Model R1 with the stacking fault relaxed by MC swaps after it has been introduced, the initial $\alpha_{initial}$ is lower than that for Model C in which the stacking fault is constrained, while both finally come to be 0, meaning a bigger destruction of SRO in Model C. $\Delta\alpha_{Co,Cr} = \alpha_{initial,\ A} - \alpha_{initial,\ B} = 0.041$. Similarly, the $\Delta\alpha$ for other atomic pairs are calculated and most of them are very close to 0 and hence negligible compared to $\Delta\alpha_{Co,Cr}$, except $\Delta\alpha_{Ni,Ni}$ which is about 0.005. The results here tally with Fig. 2(c) in that only Co-Cr and Ni-Ni segregations are significant.

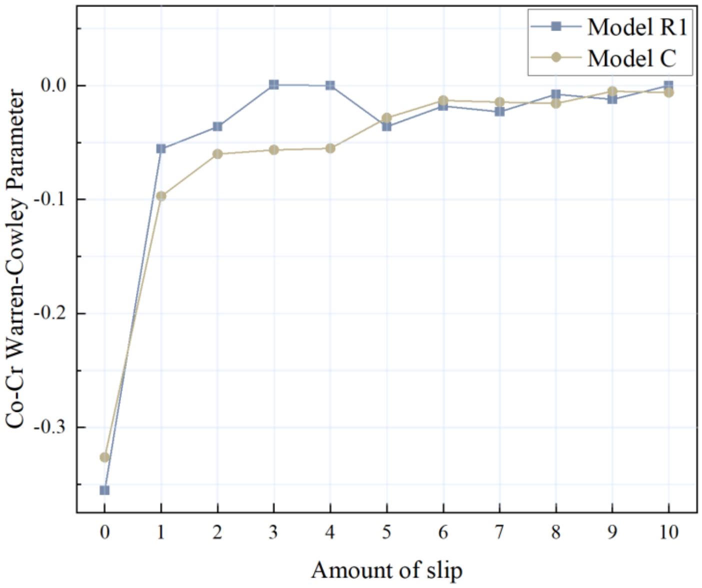

Fig. 10 Co-Cr Warren-Cowley Parameter variation for atoms in the slip plane vs slip times during the slide of the dislocations

The extra strengthening effect $\Delta\tau_{Fischer}$ from local ordering degree difference is given by (Antillon et el., 2020):

$$\Delta\tau_{Fischer} = 16\sqrt{\frac{2}{3}\sum_{A,B}\frac{m_A m_B E_{A,B}\Delta\alpha_{A,B}}{a^3}} \tag{13}$$

where m_A and m_B refer to the molar fractions of species A and B, $E_{A,B}$ is the interaction energy defined as the energy required to bring A type atom to the nearest neighbor position of B type atom (Antillon et al., 2020), and $\Delta\alpha_{A,B}$ is the local order coefficient change. Since only Co-Cr and Ni-Ni segregations are significant, then in eqn. (13) only these two pairs need to be considered. $E_{A,B}$ is about -0.0212 eV for Co-Cr atomic pair (Pei et el., 2020) and -0.002 eV for Ni-Ni atomic pair (Antillon et al., 2020), $\Delta\alpha_{Ni,Ni}$ is 0.005 and $\Delta\alpha_{Co,Cr}$ is 0.041, lattice constant a is 3.558 Å, so the Fischer strengthening is estimated from eqn. (13) to be $\Delta\tau_{Fischer} = 7.34$ MPa which is significantly lower than $\Delta\tau_{Suzuki}$.

4.3 Cottrell-Jaswon effect

In the so-called Cottrell-Jaswon effect (Cottrell and Jaswon, 1949), solute atoms preferentially cluster in the vicinity of edge dislocations driven by their stress fields, thus lowering the line tension (energy per unit length) of dislocations by an amount U_0 given by:

$$U_0 = \int_0^{2\pi} \int_0^{L} \sum_i c_i u_i r \, dr \, d\varphi \tag{14}$$

where u_i is the interaction energy between a unit length of dislocation and the solute atoms at site i, c_i is the concentration of solute atoms at site i, and L is the cut-off radius of the affected zone. The line tension decrease brought by Cottrell atmosphere is also responsible for the large geometry change of the dislocations shown in Fig. 5. In order to calculate the line tension variation and estimate the yield drop, the Gibbs free energy change in Model C and R1 during MC/MD relaxation is considered. The free energy decrease in Model R1 could be attributed to the SFE difference, the line tension difference and also the formation energy of various atomic pairs, while for Model C in which the MC/MD relaxation was done without dislocation and stacking fault, only the last term exists, but the atoms eventually reach an approximately equal ordering level as Model R1 as shown in Fig. S5(b). After removing the SFE change extracted from the SFE calculation, the line energy change is given by

$$\Delta E_{dis} = \Delta E^{Model\,R1} - \Delta E^{Model\,C} - \Delta E_{SF} \tag{15}$$

where $\Delta E^{Model\,C}$ and $\Delta E^{Model\,R1}$ are the Gibbs energy variations of Model C and R1 before and after MC swaps, ΔE_{SF} is approximately 407.8 eV, and then ΔE_{dis} is 508.8 eV. If deformation is to proceed, dislocations must increase their energy to break away from their associated solute atoms and slip into a region with randomly distributed solutes. The drag force is then given as (Dodson, 1988)

$$\Delta\tau_{Cotterell} bs = \mathrm{U}_0 = \frac{\Delta E_{dis}}{L} \tag{16}$$

where $\Delta\tau_{Cotterell}$bs is the work done for escape from the Cottrell atmosphere, L is the length of dislocations in the simulation, b is the Burgers vector of perfect edge dislocation, and s is the dislocation glide distance until all the dislocations are torn off from the Cottrell atmosphere. The *s* value chosen was 1087 Å for the following reason. Recalling in Model R1 that the trailing partial does not move until the leading partial has left the cell on one side and re-entered it from the other side, at that moment the leading partial has moved 1087 Å. So here we define *s* to be the displacement of the Peach-Koehler force ($\Delta\tau_{Cotterell}b$) for the situation when both partial dislocations have escaped from their Cottrell atmospheres, so that the work done can be equal to U_0. Then, with *s* = 1087 Å, the $\Delta\tau_{Cotterell}$ was estimated to be about 31.39 MPa.

4.4 Comparison of experimental, simulated and theoretical stress drop results

The stress drops of the different types of mechanisms discussed above are summed together and compared with the simulation results in Fig. 11. It can be seen that the Suzuki effect dominates as it takes up about 74 % of the total stress drop, while the Fisher effect accounts for the least. This finding provides us with new quantitative understanding that in f.c.c. CCAs, the Suzuki effect can have a stronger pinning effect than the Cottrell and Fisher effects due to the existence of widely extended dislocations, with large areas of stacking faults for atomic segregation and energy relaxation. As the extended dislocations move under stress, the stacking faults become constrained again, thus giving rise to large energy and stress fluctuations. Besides, the theoretical total stress drop $\Delta\tau_{Theory}$ is about 152 MPa, which is very consistent with the $\Delta\tau_{MD}$ for leading and trailing partial, with a slight discrepancy of less than 7%.

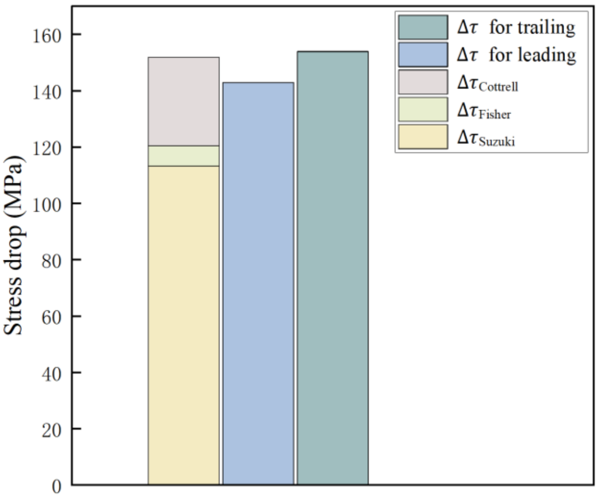

Fig. 11. Comparison of stress drop from MD simulation with theoretical prediction.

In addition, in order to validate the accuracy of the current simulations, the differences between simulations and experimental conditions are taken into account to correct the $\Delta\tau_{MD}$. Most of the tensile tests were performed on polycrystalline materials, rather than single infinite crystals subjected to shear as in our simulated cells with periodic boundary conditions, and a Taylor factor $1/m$ of 3.06 is generally used as given in eqn. (17). Furthermore, a temperature-dependent coefficient is employed to eliminate the influence of deformation temperature difference ($T_{simulation} = 1K$, $T_{experiments} = 673K$) as shown in eqn. (18), where $\beta = 0.0007$ and $\frac{\omega}{b} = 1.27$ (Li et al., 2023). Besides, constant shear force was applied in the present dynamic deformation simulation with a strain rate of approximately 1×10^{6}/s, which deviates significantly from that (~1×10^{-4}/s) in serration-reported experiments for CrCoNi-based CCAs (Antonaglia et al., 2014; Tsai et al., 2019; He et al., 2021). As shown in eqns. (19) and (20), the final stress drop can be further extrapolated by subtracting $\frac{kT}{\Delta V}\ln\left(\frac{\dot{\varepsilon}_{MD}}{\dot{\varepsilon}_{Exp}}\right)$ from $\Delta\sigma_{MD}$, with k being the Boltzmann constant, T = 673 K, $\Delta V = bdl$ being the activation volume. Here, l is taken to be 1087 Å as the distance for the escape of a dislocation from obstacles, and d = 435 Å as the mean spacing between obstacles as judged by the statistical velocity profiles of a typical dislocation line as illustrated in Fig. S6.

$$\tau = m\sigma,\ m = \cos(\varphi)\cos(\alpha) \tag{17}$$

$$\tau_{CRSS}(T_{Exp}) = \tau_{CRSS}(T_{MD})\exp\left(\frac{2\pi\omega}{b}\beta T_{MD}\right) \tag{18}$$

$$\dot{\varepsilon} = \mathrm{f}\exp\left(-\frac{\Delta F^{*} - \sigma\Delta V}{kT}\right) \tag{19}$$

$$\Delta\sigma_{Exp} = \Delta\sigma_{MD} - \frac{kT}{\Delta V}\ln\left(\frac{\dot{\varepsilon}_{MD}}{\dot{\varepsilon}_{Exp}}\right) \tag{20}$$

Then the compensation component $\frac{kT}{\Delta V}\ln\left(\frac{\dot{\varepsilon}_{MD}}{\dot{\varepsilon}_{Exp}}\right)$ is computed to be approximately 0.195 MPa and the final $\Delta\sigma_{Exp}$ estimated from simulation is nearly 10.8 MPa, that is, a little larger than the range of 5 - 10 MPa reported in experiments of CrCoNi-based CCAs (Tsai et al., 2019; Niu et al., 2017). The primary reason for the slight overestimation here could be due to the insufficient aging time for atomic diffusion in practical plastic deformation, whereas the simulated structures should have reached a rather stable state with a longer aging time. Another point worthy to note is that, according to Gerold's theory (Cao, 2022), slip passage of dislocations will break the ordering or segregation structure which is also proven in our work as shown in Fig. 8, causing a slip plane softening effect. With the strain increasing, the strengthening atomic atmospheres may not recover to their most stable states due to insufficient aging time as said before. Also, in a so-called metastable system, it will be hard to estimate and compare the stress drop from the weakened contributions of Suzuki, Fisher and Cottrell effects.

Summary

In the present work, MC/MD simulations were conducted to understand the aging process for CCAs and new atomic environments were quantitively characterized for investigation of the dynamic strain-aging mechanism. The following conclusions can be drawn:

1. The degree of Co-Cr ordering is larger in the compressive region of the edge dislocation stress field and on the slip plane, indicating a stronger Fisher pinning effect on dislocations. Besides, the heterogeneity level is determined by the stress field, which is affected by the dislocation density and annealing temperature via its effect on the stacking fault energy.
2. Dislocations tend to become straighter during formation of local atomic atmospheres. Atomic segregation was identified on stacking faults (Suzuki effect) and near dislocation cores (Cottrell effect), both of which are expected to be the source of the dynamic strain aging phenomenon in CCAs.
3. The flow stress obtained from shear tests for simulated configurations with and without new atomic environments reveals a stress drop of 143-154 MPa, which is quite consistent with the theoretically predicted value of 152 MPa. After correction for polycrystalline, strain-rate and temperature effects, the simulated stress drop is about 10.8 MPa, which is just a little higher than the stress serrations observed in experimental stress-strain curves of a lot of HEAs. Suzuki

segregation is the primary cause (~74%) of the stress drop brought by the significant reduction in stacking fault energy after segregation.

CRediT authorship contribution statement

Yuanhang Xia: Conceptualization, Investigation, Formal Analysis, Methodology, Writing - original draft, Writing – review & editing (equal). **Shuang Lyu:** Investigation, Methodology, Writing – original draft (supporting), Writing – review & editing (equal). **Wei Li:** Methodology, Validation, Formal Analysis. **Yue Chen:** Methodology, Supervision, Writing – review & editing (equal). **Alfonso H.W. Ngan:** Conceptualization, Formal analysis, Funding acquisition, Validation, Writing – original draft (supporting), Writing – review & editing (equal), Supervision

Declaration of Competing Interest

The authors declare that they have no known competing financial interests or personal relationships that could have appeared to influence the work reported in this paper.

Data availability

Data will be made available on request.

Acknowledgements

This research is supported by the National Key Research and Development Program of China (2019YFA0209904), Guangdong Province basic and applied research key project (No. 2020190718102000001), Shenzhen Fund 2021 Basic Research General Program (No. JCYJ20210324115400002), as well as the National Natural Science Foundation of China (Nos. 12102069 and 11932004). The authors are grateful for the support of research computing facilities (HPC) offered by ITS, HKU.

References

Abu-Odeh, A., Olmsted, D.L., Asta, M., 2022. Screw dislocation mobility in a face-centered cubic solid solution with short-range order. Scripta Mater. 210, 114465. https://doi.org/10.1016/j.scriptamat.2021.114465.

Antillon, E., Woodward, C., Rao, S.I., Akdim, B. and Parthasarathy, T.A., 2020. Chemical short range order strengthening in a model FCC high entropy alloy. Acta Mater. 190, 29-42. https://doi.org/10.1016/j.actamat.2020.02.041.

Antonaglia, J., Xie, X., Tang, Z., Tsai, C.W., Qiao, J.W., Zhang, Y., Laktionova, M.O., Tabachnikova, E.D., Yeh, J.W., Senkov, O.N., Gao, M.C., 2014. Temperature effects on deformation and serration behavior of high-entropy alloys (HEAs). JOM. 66, 2002-2008. https://doi.org/10.1007/s11837-014-1130-9.

Bryukhanov, I.A., 2020. Dynamics of edge dislocation in Cu–Ni solid solution alloys at atomic scale. Int. J. Plast. 135, p.102834. https://doi.org/10.1016/j.ijplas.2020.102834.

Cantor, B., Chang, I.T.H., Knight, P., Vincent, A.J.B., 2004. Microstructural development in equiatomic multicomponent alloys. Mater. Sci. Eng. A 375, 213-218. https://doi.org/10.1016/j.msea.2003.10.257.

Cao, P., 2022. Maximum strength and dislocation patterning in multi–principal element alloys. Sci. Adv. 8(45), eabq7433. https://doi.org/10.1126/sciadv.abq7433.

Chen, X., Wang, Q., Cheng, Z., Zhu, M., Zhou, H., Jiang, P., Zhou, L., Xue, Q., Yuan, F., Zhu, J., Wu, X., 2021. Direct observation of chemical short-range order in a medium-entropy alloy. Nature. 592(7856), 712-716. https://doi.org/10.1038/s41586-021-03428-z.

Chowdhury, P., Sehitoglu, H., Abuzaid, W., Maier, H.J., 2015. Mechanical response of low stacking fault energy Co–Ni alloys–Continuum, mesoscopic and atomic level treatments. Int. J. Plast. 71, 32-61. https://doi.org/10.1016/j.ijplas.2015.04.003.

Cottrell, A.H., Jaswon, M.A., 1949. Distribution of solute atoms round a slow dislocation. Proc. Math. Phys. Eng. Sci. 199(1056), 104-114. https://doi.org/10.1098/rspa.1949.0128.

Dodson, B. W., 1988. The effect of cottrell locking on structural stability in strained-layer semiconductor alloy structures. J Cryst Growth, 92(1-2), 222-232. https://doi.org/10.1016/0022-0248(88)90453-8

Fisher, J.C., 1954. On the strength of solid solution alloys. Acta Metall. 2(1), 9-10. https://doi.org/10.1016/0001-6160(54)90087-5.

Geng, J., Li, Y., Wang, F., Wang, Z., Xia, P., Li, X., Chen, D., Wang, M., Wang, H., 2023. Cyclic deformation and dynamically induced short-range ordering in small particles reinforced Al composite. Int. J. Plast. 163, 103568. https://doi.org/10.1016/j.ijplas.2023.103568.

Gludovatz, B., Hohenwarter, A., Thurston, K.V., Bei, H., Wu, Z., George, E.P., Ritchie, R.O., 2016. Exceptional damage-tolerance of a medium-entropy alloy CrCoNi at cryogenic temperatures. Nat. Commun. 7(1), 10602. https://doi.org/10.1038/ncomms10602.

He, H., Naeem, M., Zhang, F., Zhao, Y., Harjo, S., Kawasaki, T., Wang, B., Wu, X., Lan, S., Wu, Z., Yin, W., 2021. Stacking fault driven phase transformation in CrCoNi medium entropy alloy. Nano Lett. 21(3), 1419-1426. https://doi.org/10.1021/acs.nanolett.0c04244.

Hua, D., Xia, Q., Wang, W., Zhou, Q., Li, S., Qian, D., Shi, J., Wang, H., 2021. Atomistic insights into the deformation mechanism of a CoCrNi medium entropy alloy under nanoindentation. Int. J. Plast. 142, 102997. https://doi.org/10.1016/j.ijplas.2021.102997.

Hull, D., Bacon, D.J., 1984. Strength of crystalline solids. In: Introduction to dislocations, 3rd Ed.

Pergamon Press Ltd.: Oxford, U.K.

Kang, J.H., Ingendahl, T., von Appen, J., Dronskowski, R., Bleck, W., 2014. Impact of short-range ordering on yield strength of high manganese austenitic steels. Mater. Sci. Eng. A 614, 122-128. https://doi.org/10.1016/J.MSEA.2014.07.016.

Kaushik, L., Kim, M.S., Singh, J., Kang, J.H., Heo, Y.U., Suh, J.Y., Choi, S.H., 2021. Deformation mechanisms and texture evolution in high entropy alloy during cold rolling. Int. J. Plast. 141, 102989. https://doi.org/10.1016/j.ijplas.2021.102989.

Li, Q.J., Sheng, H., Ma, E., 2019. Strengthening in multi-principal element alloys with local-chemical-order roughened dislocation pathways. Nat. Commun. 10(1), 3563. https://doi.org/10.1038/s41467-019-11464-7.

Li, W., Lyu, S., Chen, Y., Ngan, A.H., 2023. Fluctuations in local shear-fault energy produce unique and dominating strengthening in metastable complex concentrated alloys. Proc. Natl. Acad. Sci. 120(12), e2209188120. https://doi.org/10.1073/pnas.2209188120.

Marchenko, A., Maziere, M., Forest, S., Strudel, J.L., 2016. Crystal plasticity simulation of strain aging phenomena in α-titanium at room temperature. Int. J. Plast. 85, 1-33. https://doi.org/10.1016/j.ijplas.2016.05.007.

Niu, S., Kou, H., Zhang, Y., Wang, J., Li, J., 2017. The characteristics of serration in Al0.5CoCrFeNi high entropy alloy. Mater. Sci. Eng. A. 702, 96-103. https://doi.org/10.1016/j.msea.2017.05.075.

Pei, Z., Li, R., Gao, M.C., Stocks, G.M., 2020. Statistics of the NiCoCr medium-entropy alloy: Novel aspects of an old puzzle. NPJ Comput. Mater. 6(1), 122. https://doi.org/10.1038/s41524-020-00389-1.

Plimpton, S., 1995. Fast parallel algorithms for short-range molecular dynamics. J. Comput. Phys. 117(1), 1-19. https://doi.org/10.1006/jcph.1995.1039.

Smith, L.T., Su, Y., Xu, S., Hunter, A., Beyerlein, I.J., 2020. The effect of local chemical ordering on Frank-Read source activation in a refractory multi-principal element alloy. Int. J. Plast. 134, 102850. https://doi.org/10.1016/j.ijplas.2020.102850.

Snoek, J.L., 1942. Tetragonal martensite and elastic after effect in iron. Physica. 9(8), 862-864. https://doi.org/10.1016/S0031-8914(42)80061-0.

Song, Q., Li, Z., Zhu, Y., Huang, M., 2018. On the interaction of solute atoms with circular inhomogeneity and edge dislocation. Int. J. Plast. 111, 266-287. https://doi.org/10.1016/j.ijplas.2018.07.019.

Su, Z., Shi, T., Shen, H., Jiang, L., Wu, L., Song, M., Li, Z., Wang, S., Lu, C., 2022. Radiation-assisted chemical short-range order formation in high-entropy alloys. Scripta Mater. 212, 114547. https://doi.org/10.1016/j.scriptamat.2022.114547.

Suzuki, H., 1952. Chemical interaction of solute atoms with dislocations. Sci. Rep. Res. Inst. Tohoku Univ. A 4, 455-463.

Tsai, C.W., Lee, C., Lin, P.T., Xie, X., Chen, S., Carroll, R., LeBlanc, M., Brinkman, B.A., Liaw, P.K., Dahmen, K.A., Yeh, J.W., 2019. Portevin-Le Chatelier mechanism in face-centered-cubic metallic alloys from low to high entropy. Int. J. Plast. 122, 212-224. https://doi.org/10.1016/j.ijplas.2019.07.003.

Wang, C., Sun, C., Cai, W., Qian, L., Guo, X., Fu, M.W., 2022. Evolution of partial dislocation slip–mediated deformation twins in single crystals: a discrete dislocation plasticity model and an analytical approach. Int. J. Plast. 152, 103230. https://doi.org/10.1016/j.ijplas.2022.103230.

Wang, J., Jiang, P., Yuan, F., Wu, X., 2022. Chemical medium-range order in a medium-entropy alloy.

Nat. Commun. 13(1), 1021. https://doi.org/10.1038/s41467-022-28687-w.

Xie, Z., Jian, W.R., Xu, S., Beyerlein, I.J., Zhang, X., Yao, X., Zhang, R., 2022. Phase transition in medium entropy alloy CoCrNi under quasi-isentropic compression. Int. J. Plast. 157, 103389. https://doi.org/10.1016/j.ijplas.2022.103389.

Záležák, T., Svoboda, J., Dlouhý, A., 2017. High temperature dislocation processes in precipitation hardened crystals investigated by a 3D discrete dislocation dynamics. Int. J. Plast. 97, 1-23. https://doi.org/10.1016/j.ijplas.2017.04.017.

Zhang, R., Zhao, S., Ding, J., Chong, Y., Jia, T., Ophus, C., Asta, M., Ritchie, R.O., Minor, A.M., 2020. Short-range order and its impact on the CrCoNi medium-entropy alloy. Nature. 581(7808), 283-287. https://doi.org/10.1038/s41586-020-2275-z.

Zhou, L., Wang, Q., Wang, J., Chen, X., Jiang, P., Zhou, H., Yuan, F., Wu, X., Cheng, Z., Ma, E., 2022. Atomic-scale evidence of chemical short-range order in CrCoNi medium-entropy alloy. Acta Mater. 224, 117490. https://doi.org/10.1016/j.actamat.2021.117490.